Wideband Flush-Mounted Surface Wave Antenna of Very Low Profile

Zhuozhu Chen, *Student Member, IEEE*, and Zhongxiang Shen, *Senior Member, IEEE*

***Abstract*—This paper presents the design of a compact and wideband surface wave antenna that exhibits very low profile and can be flush-mounted on a conformal platform. The proposed antenna comprises a tapered grounded ceramic slab, a unidirectional surface wave launcher, and a tapered impedance transition. The ceramic slab is smoothly tapered to transform the guided surface wave into radiated space wave over a wide frequency range. The surface wave launcher employs a probe-fed parallel plate waveguide with a modified parabolic reflecting wall and a metallic post, which are critical for effectively transforming the cylindrical waves to a unidirectional plane wave within a broad frequency range. Simulated results show that the proposed surface wave antenna achieves a wide operation bandwidth from 6.1 GHz to 18 GHz with a thickness of only 0.12 λ_0 at the center frequency. Acceptable gain values with stable and quasi end-fire radiation beams are obtained over the entire frequency band. A prototype of the proposed antenna is fabricated and tested. Measured results are in good agreement with simulated ones.**

***Index Terms*— Flush-mounted, low-profile, surface wave antenna, surface wave launcher, wideband antenna.**

I. Introduction

RECENT years have witnessed a growing demand for wideband and low-profile end-fire antennas, which can be flush-mounted for aircraft, missile, and unmanned aerial vehicle (UAV) applications. Traditional end-fire antennas such as log-periodic [1], Yagi-Uda [2], and tapered slot antennas [3] can achieve wide bandwidth. However, they are not suitable to be mounted on the surfaces of airborne applications because the mounting platforms have a significant effect on the antenna performance. Although cavity-backed structures can be utilized to mitigate the ground effects, the depth of the cavity needs to be a quarter-wavelength [4], which limits the structures for low-profile applications.

Surface wave antennas based on dielectric slabs exhibit the advantages of low profile, moderate gain with end-fire radiation, and structurally conformal to airborne installations with good aerodynamic characteristics [5]-[7]. In surface wave antennas, surface waves propagate along the antenna surfaces and radiate into free space at discontinuities or when a surface wave gap is produced [8], [9]. Surface wave launchers play an important role on the performance of such antennas. One of the suitable candidates for TM_0 mode surface wave excitation in grounded slab is the slot Yagi-Uda antenna launcher [10], [11]. However, the bandwidth of the slot-based launcher is generally narrow due to its resonant nature. Other typical feeding devices widely used in surface wave antennas are rectangular waveguides and flare horns [12]. Nevertheless, a poor impedance matching will be introduced when the dielectric thickness is very low [13], [14], which may limit these feeding structures for wideband and low-profile applications. Ridged structures are often employed to increase the bandwidth [15]-[17]. In [16], a flared slot antenna can achieve stable radiation beam near the end-fire direction over a 4:1 frequency band. However, the antenna thickness is $0.32\lambda_0$ at the center frequency, which is relatively thick.

It is known that simultaneously achieving a wide bandwidth and retaining a small thickness remain a challenging task for surface wave antennas. In this paper, a wideband, low-profile and compact surface wave launcher is proposed to feed the grounded tapered dielectric slab of high dielectric constant. The proposed launcher employs a probe-fed parallel-plate waveguide with a modified parabolic reflecting wall and a metallic post. The metallic post is placed close to the feeding probe to serves as a matching element, which is essential for improving the impedance matching of the launcher. The shape of the parabolic reflecting wall is carefully modified so as to obtain a more uniform amplitude and phase distribution over a wide bandwidth. The fractional bandwidth of our surface wave antenna is 100%, the antenna thickness is only $0.12\lambda_0$, and its volume is $0.45\lambda_0^3$ at the center frequency.

The proposed surface wave antenna has the following advantages. 1) The antenna can achieve a wide bandwidth while maintaining a very low profile and compact size. 2) Stable and quasi end-fire radiation beams with moderate gain values are obtained over the entire operating band. 3) The antenna is structurally simple and conductor-backed, which is potentially useful to be conformal and flush-mounted for missile and unmanned aerial vehicle applications.

II. Antenna Configuration

Fig. 1 shows the configuration of our proposed wideband and low-profile surface wave antenna. It consists of a wideband probe-fed unidirectional surface wave launcher, a tapered grounded ceramic slab, and a tapered impedance transition. The launcher and slab are seamlessly joined together by tapering one end of both parts. The length and width of the antenna are denoted by *L* and *W*, respectively.

Manuscript received Nov 7, 2014.

The authors are with the School of Electrical and Electronic Engineering, Nanyang Technological University, Singapore 639798, Singapore (e-mail: chen0855@e.ntu.edu.sg; ezxshen@ntu.edu.sg).

Color versions of one or more of the figures in this paper are available online at http://ieeexplore.ieee.org.

Digital Object Identifier

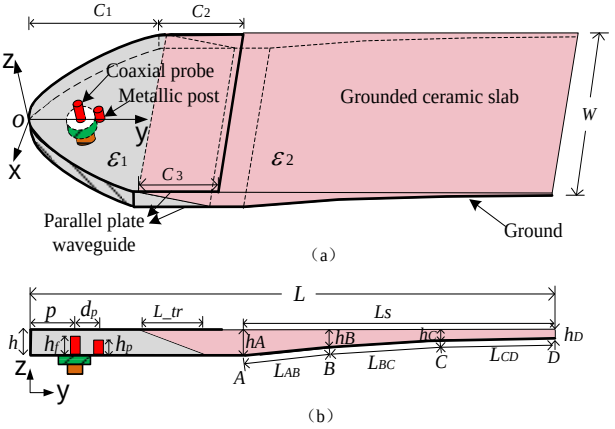

Fig. 1. Configuration of the proposed wideband, low-profile, and compact surface wave antenna, (a) perspective view, (b) side view.

The surface wave launcher consists of a coaxial-to-parallel plate waveguide transition with a modified parabolic reflecting wall and a metallic post. The shape of the reflecting wall can be expressed as $|x| = (4py)^n$. The distance between the coaxial probe and the reflecting wall is *p*. The coaxial probe and metallic post are located along the symmetric plane of the launcher with a separation of d_p, and they protrude into the substrate with heights of h_f and h_p, respectively.

The grounded slab is smoothly tapered to transform the surface wave into radiated space wave as well as to improve the matching condition between dielectric slab and free space. As shown in Fig. 1(b), the taper is mainly determined by three segments *AB*, *BC*, and *CD*. The lengths of these three segments are represented by L_{AB}, L_{BC}, and L_{CD}, respectively. The thicknesses of the slab at points *A*, *B*, *C*, and *D* are denoted by h_A, h_B, h_C, and h_D, respectively. By selecting the proper length of each segment and thickness at each point, the curvature of the ground can be controlled. It should be mentioned that the ground curvature has a significant effect on the sidelobe levels of the radiation patterns, and it can also be controlled by employing more segments or other arc-shaped tapers. In our design, three linear segments are used in order to facilitate simulation and fabrication.

III. Design Considerations

A. Tapered Grounded Dielectric Slab

It is well-known that a grounded dielectric slab can support the propagation of surface waves. As shown in Fig. 2, assume that a uniformly grounded dielectric slab is infinite in the *x* and *y* directions, the propagation is along the +*y* direction and fields have no variation in the *x* direction. The lossless slab is of thickness *h* in the +z direction and has a relative permittivity of ε_r. The following relation is obvious [8]

$$\beta_y^2 = k_0^2 + \alpha_z^2 \tag{1}$$

where β_y is the phase constant of a surface wave in the +*y* direction, k_0 represents the wave number in free space, α_z denotes the attenuation constant in the +*z* direction. Due to the fact that the field exponentially decays in air away from the dielectric surface, surface waves are intrinsically bound onto the dielectric interface.

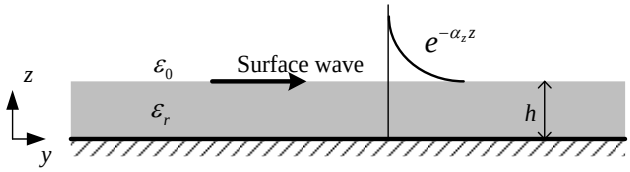

Fig. 2. Surface wave bound onto a uniform grounded dielectric interface, decaying exponentially away from the surface.

For the dominant TM_0 mode propagating in the grounded dielectric slab, the propagation constant β_y satisfies [18]

$$k_1 tan(k_1 h) = \varepsilon_r k_2 \tag{2}$$

$$k_1{}^2 + k_2{}^2 = (\varepsilon_r - 1)k_0{}^2 \tag{3}$$

where $k_1{}^2 = \varepsilon_r k_0{}^2 - \beta_y{}^2$ and $k_2{}^2 = \beta_y{}^2 - k_0{}^2$.

The power inside and outside the dielectric of the uniform grounded slab can be derived as [19]

$$P_1|_{z=0}^{z=h} = K_Y^2 \frac{1}{4k_1}\frac{\beta_y}{\omega\varepsilon_r}[k_1 h + \frac{1}{2}sin(2k_1 h)] \tag{4}$$

$$P_2|_{z=h}^{z=\infty} = K_Y^2 \frac{1}{4\varepsilon_r}\frac{k_1^2}{k_2^3}\frac{\beta_y}{\omega\varepsilon_r} sin^2(k_1 h) \tag{5}$$

where K_Y is a coefficient that is equal to the y-directed current per unit depth in the *x* direction. The subscripts 1 and 2 represent the dielectric and air regions, respectively. $P_1|_{z=0}^{z=h}$ is the power integrated from the plane *z* = 0 to *z* = *h*, which denotes the total power inside the dielectric. $P_2|_{z=h}^{z=\infty}$ is the power residing outside the dielectric.

The power ratio *C* that represents the power inside the slab $P_1|_{z=0}^{z=h}$ over the total power ($P_1|_{z=0}^{z=h} + P_2|_{z=h}^{z=\infty}$) can be calculated as

$$C = \frac{\varepsilon_r k_2^3[2k_1 h + sin(2k_1 h)]}{\varepsilon_r k_2^3[2k_1 h + sin(2k_1 h)] + 2k_1^3 sin^2(k_1 h)} \tag{6}$$

It is generally required that most of surface wave power can be retained inside the dielectric slab right after it enters the tapered grounded slab from a parallel-plate waveguide. This can eliminate the strong reflection and potential diffraction occurring at the feeding junction, which may degrade the radiation pattern. It is clear from (6) that the power ratio C is related to slab thickness *h*, dielectric constant ε_r , and wavelength λ, and this relationship is shown in Fig. 3. It is noted that the power ratios inside the slab are around 0.6 when the slab thickness is $h = \lambda/4\sqrt{\varepsilon_r}$ for different dielectric constants. As the slab thickness increases, the power ratio *C* increases meaning that more power is concentrated inside the slab. Generally speaking, the value of *C* above 0.9 is sufficient for minimizing the reflection and diffraction at the feeding junction [20].

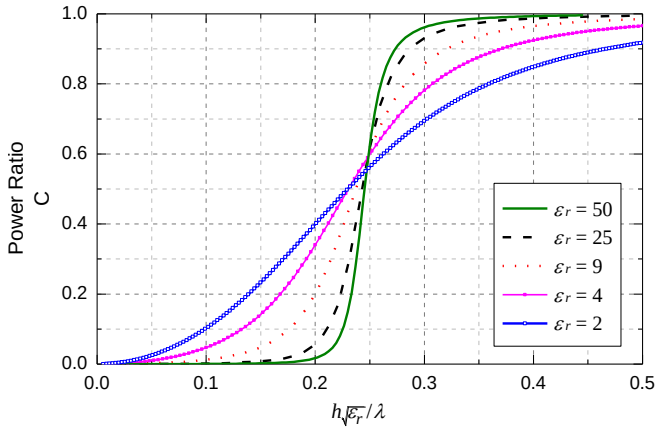

Fig. 3. Relationship of power ratio *C*, slab thickness, dielectric constant, and wavelength.

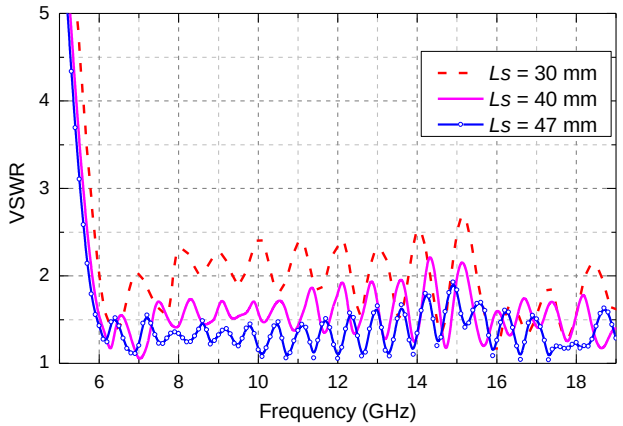

Fig. 4. Effects of *Ls* on VSWR of the linearly tapered grounded slab (h_A = 3 mm, h_D = 0.2 mm, *W* = 29 mm, ε_r = 25).

TABLE I
SIDELOBE LEVELS (SLLS) COMPARISON OF THE LINEARLY TAPERED SLAB (#1: h_A = 3 mm, h_D = 0.2 mm, L_s= 47 mm) AND THREE-SEGMENT TAPERED SLAB (#2: h_A = 3 mm, h_B = 2.1 mm, h_C = 1 mm, h_D = 0.2 mm, L_{AB} = 11 mm, L_{BC} = 15.5 mm, L_{CD} = 20.5 mm).

f (GHz)		<12	12	14	16	18
#1 SLL (dB)	E-plane	-	-7.5	-7	-2.6	-5
	H-plane	-	-9	-12.9	-13	-17
#2 SLL (dB)	E-plane	-	-8.5	-8.3	-9.5	-9.1
	H-plane	-	-12.7	-13.3	-17.8	-16.2

Although surface waves are bound waves, they can radiate into free space once a discontinuity occurs or a surface wave gap is produced. When looking straight down from the +z direction, the grounded dielectric slab can be regarded as a transmission line, which is shorted at the bottom. For the tapered grounded slab, the surface impedance alters continuously as the height changes smoothly. When the slab height reaches $\lambda/4\sqrt{\varepsilon_r}$, the short circuit at the bottom end is transformed into an open circuit at the interface. At this resonant point, the guided surface wave can be effectively transformed into a space wave that can be radiated into space [9].

In order to effectively transform the surface wave into radiated space wave over a wide frequency band, a large range of thickness should be selected for the dielectric slab for a given ε_r. On the other hand, the slab thickness should be maintained low so that a compact and low-profile antenna can be designed, which indicates that a large ε_r should be selected. Finally, a tapered grounded dielectric slab with a high dielectric constant ε_r is employed to design a wideband and low-profile surface wave antenna.

The tapered grounded slab radiator can be designed based on the above understandings, and the procedures are summarized below.

i) The antenna height h_A and dielectric constant ε_r of the tapered slab can be first determined once the starting frequency f_{min} of the operating band is specified. In our design, the bandwidth from 6 GHz to 18 GHz is desired and a large ε_r is preferred to maintain a low profile. h_A should satisfy

$$h_A > \lambda_{min}/4\sqrt{\varepsilon_r} \tag{7}$$

where λ_{min} is the free-space wavelength at the starting frequency f_{min}. Meanwhile, it is desirable that the power ratio *C* at the beginning part of the tapered slab is larger than 0.9. Based on the above, we select a ceramic slab with a high dielectric constant ε_r =25 and height h_A = 3mm. In this case, the power ratio *C* is 0.93 so that the reflection and diffraction at the feeding junction can be negligible.

ii) Next, the slab width *W* can be determined based on the desired beamwidth in the H-plane. For the TM surface wave propagating in the grounded dielectric slab, it is assumed that the field distribution is uniform along the *x* direction, as shown in Fig. 2. The half-power beamwidth (HPBW) of the radiation pattern in the H-plane is approximately [21]

$$\Theta_h = 114.6 sin^{-1}\left(\frac{0.443\lambda}{W}\right) \text{ degrees} \tag{8}$$

In our example, the slab width is selected to be 29 mm so that the HPBW is around 45^0at the center frequency *f* = 12 GHz.

iii) Furthermore, the length L_s of the tapered slab can be initially determined by considering both the beam tilt-angle in the E-plane and the impedance matching condition between the dielectric slab and free space. The guided surface waves can be radiated into free space at the resonant position of the tapered grounded slab, where the slab thickness is $\lambda/4\sqrt{\varepsilon_r}$. Therefore, the region starting from the resonant point to the end of the slab can be considered as an extended ground plane, whose length L_g affects the beam tilt-angle of the pattern in the E-plane [8]. As L_g increases, the beam angle tilts closer to the end-fire direction. When $Lg \cong 0.8\lambda$, the radiation beam is around 45^0 away from the end-fire direction.

On the other hand, in order to smoothen the impedance transition from the dielectric slab to free space, a longer length L_s is preferred and h_D is better kept small to widen the bandwidth though it may be limited by the fabrication constrains. However, a long slab takes up more space and leads to a less compact structure. Therefore, a suitable length should be selected to compromise the matching condition and compactness. As a simple instance, a waveport is placed at the thick side of the tapered slab for excitation using ANSYS High Frequency Structure Simulator (HFSS). The initial parameters are ε_r = 25, h_A = 3 mm, h_D = 0.2 mm, *W* = 29 mm. The effects of slab length *Ls* on the port's voltage standing wave ratio

(VSWR) are shown in Fig. 4. It is seen that a lower VSWR is obtained as L_s increases. When L_s is 47 mm, the VSWR value remains less than 2 within the entire frequency range. Thus, L_s can be initially selected to be 47mm considering both the beam angle and matching condition in our design.

iv) Finally, the curvature of the ground can be carefully designed by considering the sidelobe level (SLL) of the radiation pattern. Since the ground shape affects the surface impedance variation along the tapered slab and the field distribution along the surface, it plays a significant role on the radiation pattern, especially for the SLL [20], [22]. A simple way to control the curvature is to divide the tapered ground into several segments, and then vary the length and slope of each segment properly. In our design, three segments are employed in order to simplify the simulation. In the simulated model, the SLL of the tapered slab is treated as the objective of the optimization problem, which is a function of six parameters h_A, h_B, h_C, L_{AB}, L_{BC}, L_{CD}, and the operating frequency. Within a reasonable range of values, all these parameters are carefully tuned and finalized to obtain an acceptable SLL over the entire band. After optimization, the final parameters are h_A = 3 mm, h_B = 2.1 mm, h_C = 1 mm, h_D = 0.2 mm, L_{AB} = 11 mm, L_{BC} = 15.5 mm, and L_{CD} = 20.5 mm. It should be mentioned that using more segments or arc-shaped ground may also result in a satisfactory result. However, this can increase the complexity of design and fabrication, and the simulation process may also be time-consuming.

In order to illustrate the significances of the ground curvature on the radiation patterns, we summarized the comparison of sidelobe levels (SLLs) of the linearly tapered slab (#1) and the three-segment one (#2) in Table I. The E-plane is the y-z plane, and the H-plane is the plane orthogonal to E-plane and includes the maximum beam peak. At lower frequencies, the radiation beams are wide and no sidelobes appear. Therefore, Table I only lists the SLLs at frequencies larger than 12 GHz. It is seen that the SLLs of the E-plane are large at higher frequencies for the linearly tapered grounded slab. In comparison, they are effectively improved for the three-segment taper. It is worth mentioning that the gain values of the three-segment taper are slightly larger than the linearly tapered one with the improvement in SLL at higher frequencies. In addition, slight change of the ground shape has little effect on the VSWR of the slab since a good impedance matching is mainly obtained by employing a sufficiently long tapered structure. Therefore, the VSWR is almost unchanged by employing a three-segment tapered slab compared to the linearly tapered one.

As discussed, surface waves are bound onto the interface of the tapered grounded dielectric slab. However, they can be transformed into radiated space waves efficiently in the tapered structure when the slab thickness reaches $\lambda/4\sqrt{\varepsilon_r}$. As a proof of concept, a waveport is used to excite the tapered grounded dielectric slab. Fig. 5 shows the electric field distributions of the tapered grounded dielectric slab and in free space at different frequencies, which clearly illustrates the transformation from guided surface waves to radiated space wave via the tapered structure. As seen, the areas showing the strongest electric field intensity of the tapered slab effectively transform the surface waves into space wave, while the areas before that, starting from the waveport, guide the waves. The radiation occurs at different thicknesses of the tapered slab at different frequencies, the corresponding thickness is $\lambda/4\sqrt{\varepsilon_r}$, as expected.

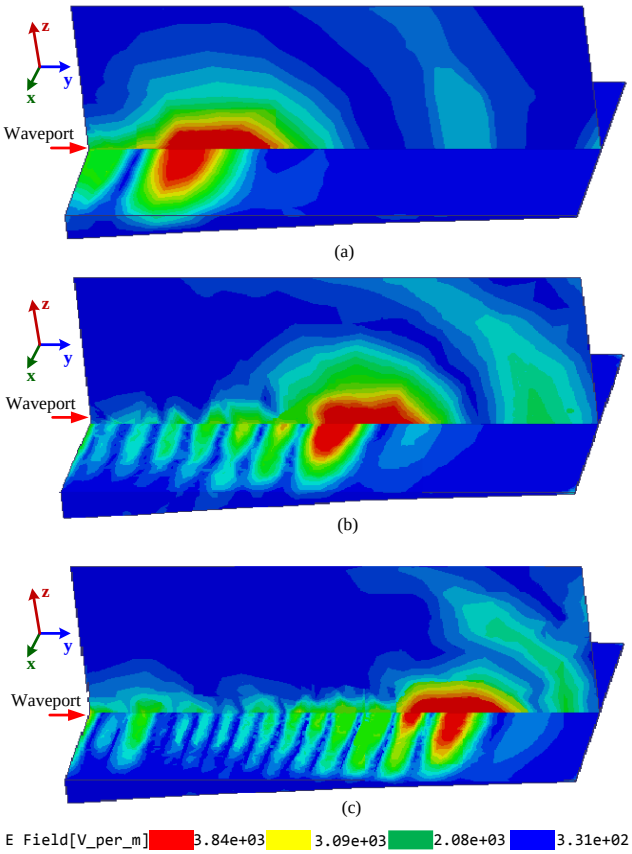

Fig. 5. E-Field distributions of the tapered grounded dielectric slab and in free space at different frequencies, (a) 6 GHz, (b) 12 GHz, (c) 18 GHz.

B. Surface Wave Launcher

The surface wave launcher is designed based on the following considerations. First, a broad bandwidth should be obtained when the structure maintains a very low profile. Second, in order to improve the launching efficiency, it is required that the phase differences between waves arriving at the waveguide aperture is minimized, and it is desirable to obtain a uniform distribution of the electric field at the waveguide aperture as well. Therefore, the cylindrical waves excited by the coaxial probe should be transformed to unidirectional quasi-plane waves efficiently.

A few strategies are employed in our structure to meet the aforementioned requirements. The center frequency of our designed antenna is f_0 = 12 GHz. A Teflon sheet with a low permittivity of 2.1 is used as the slab in the parallel-plate waveguide because has the same dielectric constant as the Teflon material inside the SMA feed. The thickness is selected to be 3mm, which is the same height as the grounded tapered slab. The top, bottom, and reflecting walls of the Teflon are covered with copper tapes to form the parallel-plate waveguide, which supports the propagation of the quasi-TEM wave.

1) Metallic Post

In the launcher, a metallic post is utilized to serves as a matching element, which helps to broaden the bandwidth of the

launcher to a certain extent. The post partially penetrating into the waveguide acts as a shunt capacitive reactance, whose value is related to the height and diameter of the post. The mutual coupling between the coaxial probe and the post is determined by their spacing. By varying the length, diameter, and location of the post, the self-impedance of the metallic post and the mutual impedance between the probe and post can be adjusted. This can affect the input impedance of the launcher and help to improve the impedance matching. Fig. 6 shows the simulated VSWR of our proposed surface wave launcher with and without the metallic post. The VSWR is above 1.8 over frequency range without the post. However, the value is much lower with a metallic post of suitable height and at an appropriate location, which indicates that the impedance matching is significantly improved.

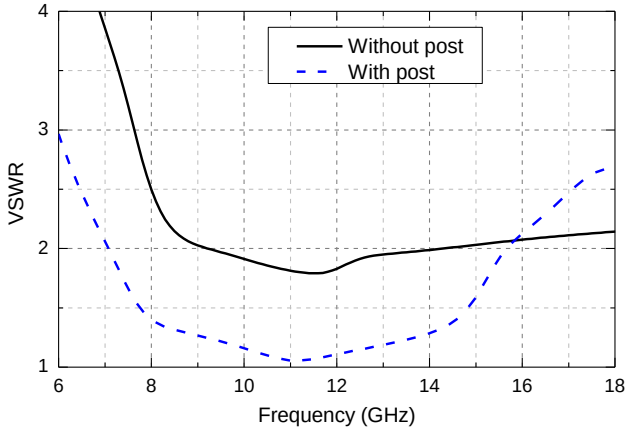

Fig. 6. Effects of metallic post on VSWR of the launcher. (ε_r = 2.1, h = 3 mm, W = 29.1 mm, n = 0.5, h_f = 2.85 mm, p = 4.3 mm).

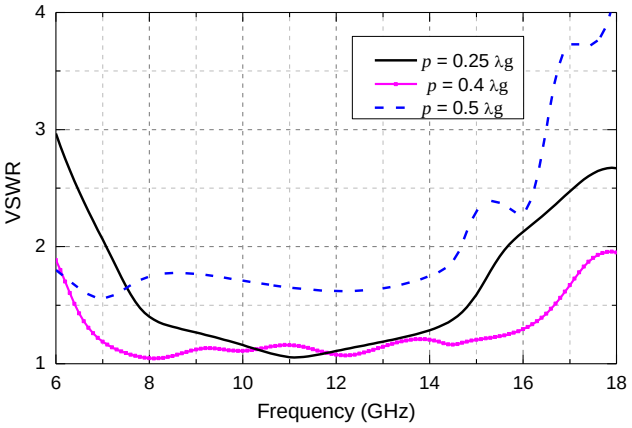

Fig. 7. Effects of distance p on VSWR of the launcher. (ε_r = 2.1, h = 3 mm, W = 29.1 mm, n = 0.5, h_f = 2.85 mm, d_p = 2.4 mm, h_p = 1.7 mm).

2) Reflecting Wall

The coaxial probe is fed at the focal point of the parabolic reflecting wall. The focal length p is generally chosen to be a quarter guided wavelength λ_g at the center frequency for matching purpose [13]. However, by varying p to be larger than a quarter but less than a half guided wavelength λ_g at the center frequency helps to widen the bandwidth [23]. Fig. 7 shows the effects of the distance p on the VSWR of the launcher. It is seen that the operating frequency ranges from 7 GHz to 15.8 GHz for VSWR less than 2 when $p = 0.25\lambda_g$. By increasing the distance p to be $0.4\lambda_g$, the frequency band from 6 GHz to 18 GHz for VSWR ≤ 2 can be achieved. When p is larger than $0.5\lambda_g$, the impedance matching degrades.

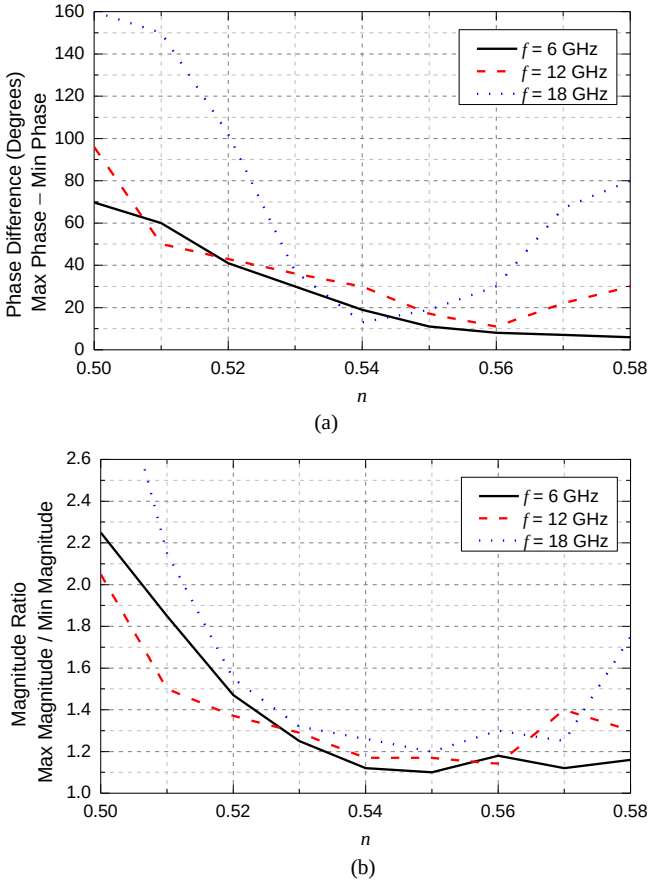

Fig. 8. Simulated (a) phase differences between the maximum and minimum phase values and (b) magnitude ratios of the maximum to minimum magnitude values of the electric field along the aperture width of the waveguide as a function of n at different frequencies. (ε_r = 2.1, h = 3 mm, W = 29.1 mm, p = 6.8mm, h_f = 2.85 mm, d_p = 2.4 mm, h_p = 1.7 mm).

A modified parabolic reflecting wall is employed to transform the cylindrical waves excited by the probe to quasi-plane waves at the aperture of the parallel plate waveguide. The shape of reflecting wall is optimized by carefully choosing the value n properly. It is well known that based on the geometric optics, when a source is positioned at the focal point and excited unidirectionally towards a large parabolic reflector, the reflected wave is planar [24]-[26]. However, different from the ideal case, a coaxial probe in our proposed structure excites an omni-directional cylindrical wave rather than a unidirectional one. Therefore, there exists wave superposition of the reflected wave and the wave transmitted directly from the probe in the launcher, leading to an unavoidable phase distortion at the aperture of the parallel plate waveguide. Due to the very compact size of our launcher, using geometrical optics is insufficient to analyze the phase distortion caused by the wave superposition of the structure. To illustrate the importance of the shape of the reflecting wall, we plot the effects of n on the phase and magnitude errors provided by the launcher with the aid of HFSS, as shown in Fig. 8.

Fig. 8(a) plots the differences between the maximum and minimum phase values of the electric field distribution along aperture width of the parallel plate waveguide. It is seen that the phase differences are large for the ideally parabolic shape with n = 0.5. However, the phase distortion can be well improved by varying n properly. When n approaches 0.55, the phase differences can be maintained below 20° within the whole frequency band. Fig. 8(b) shows the corresponding ratios of the maximum to minimum magnitude values as a function of n. It is noticed that the magnitude ratios follow almost the same variations as the phase difference, and the values are below 1.2 at different frequencies when n = 0.55. Therefore, it is concluded that quasi-plane waves are obtained in our proposed launcher for the case of n = 0.55 considering both the phase and magnitude errors. It is worth noting that choosing a certain value of n may not account for the lowest phase and magnitude differences at all frequencies. Therefore, an appropriate value of n should be chosen to yield a good compromise of phase and magnitude differences over the entire band.

Based on the above discussions, the following procedures may be considered to design the proposed wideband and low-profile surface wave launcher.

i) Choose a substrate with the same dielectric constant ε_r as the insulating material in the feeding probe and the same height as the tapered grounded dielectric slab.

ii) As an initial start, use the ideally parabolic wall with n = 0.5. The coaxial probe is fed at the focal point with $p = \lambda_g/4$, where λ_g is the guided wavelength at the center frequency f_0. The focal length p can be larger than $\lambda_g/4$, but less than $\lambda_g/2$ to maximize the bandwidth. The parabolic shape may also be optimized by studying the variation of the phase and magnitude errors at the waveguide aperture at different frequencies.

iii) Employ a metallic post to improve the impedance matching.

A few iterations may be invoked to obtain an optimum design. The final dimensions of our proposed surface wave launcher are as follows: $\varepsilon_r = 2.1$, h = 3 mm, n = 0.55, p = 6.8mm, h_f = 2.85 mm, W = 29.1 mm, d_p = 2.4 mm, h_p = 1.7 mm, C_1 = 17.8 mm, C_2 = 30 mm. The diameters of the coaxial probe and metallic post are both 1.3 mm.

C. Tapered Impedance Transition

In order to realize a smooth impedance transition between the Teflon slab and ceramic slab, one end of each slab is tapered, and the two parts are seamlessly connected, as shown in Fig. 9. ε_1 and ε_2 represent the dielectric constants of Teflon and ceramic materials, respectively. h_1 and h_2 denote the corresponding dielectric heights. L_tr is the length of the transition part.

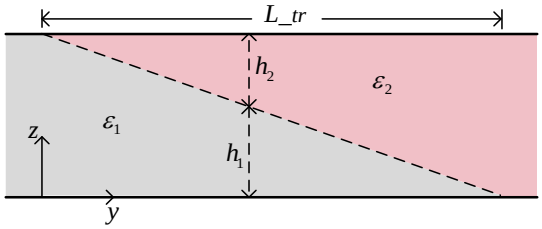

Fig. 9. Side view of the tapered impedance transition.

The propagation phase constant in the tapered transmission line can be approximately expressed as [27], [28]

$$\beta_g = \frac{2\pi}{\lambda_0}\sqrt{\varepsilon_a} \tag{9}$$

where

$$\varepsilon_a = \frac{\varepsilon_1 h_1 + \varepsilon_2 h_2}{h_1 + h_2} \tag{10}$$

is the volume average dielectric constant in the transition, λ_0 is the wavelength in free space.

The electrical length of the tapered transmission line is derived as

$$\phi = \int_0^{L\_tr} \beta_g \, dy = \frac{4\pi(\varepsilon_2^{1.5} - \varepsilon_1^{1.5})}{3\lambda_0(\varepsilon_2 - \varepsilon_1)} L\_tr \tag{11}$$

For the tapered transmission line, when the electrical length ϕ is greater than 3π, the reflection coefficient is quite small [29]. In our proposed structure, the center frequency f_0 is used to determine the transition length L_tr. Based on (11), L_tr is calculated to be 10.5 mm if ϕ is equal to 3π at f_0 = 12 GHz. Therefore, the length is selected to be L_tr = 10.5 mm in order to obtain a good matching as well as to maintain a relatively short length for the sake of compactness.

IV. Antenna Performance

A prototype of our proposed surface wave antenna is shown in Fig. 10. A ceramic material with a high dielectric constant of ε_r = 25 and loss tangent of $\tan\delta = 0.0002$ is used for the grounded tapered radiator. The surface wave launcher is fabricated using a Teflon sheet. The Teflon and ceramic parts are seamlessly glued together and covered by copper tapes on both top and bottom sides of the antenna. The reflecting wall of the Teflon part is also covered with copper tape. The dimensions of our proposed antenna are designed to be: n = 0.55, p = 6.8, L = 80.3 mm, W = 29.1mm, C_1 = 16.7 mm, C_2 = 13.2 mm, C_3 = 12.2 mm, d_p = 2.4 mm, h_f= 2.85 mm, h_p = 1.7 mm, L_tr = 10.5 mm, h_A = 3 mm, h_B = 2.1 mm, h_C = 1 mm, h_D = 0.2 mm, L_{AB} = 11 mm, L_{BC} = 15.5 mm, L_{CD} = 20.5 mm.

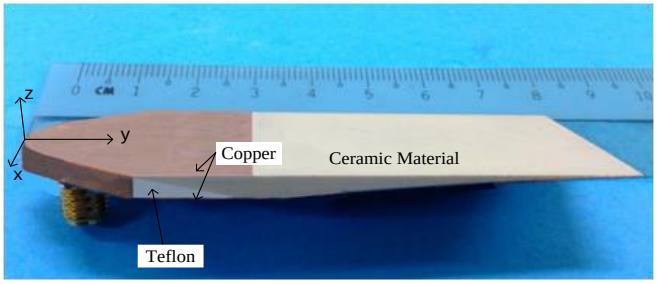

Fig. 10. Prototype of the proposed surface wave antenna.

Fig. 11 shows the simulated and measured VSWR results of the proposed surface wave antenna. It is seen that a wide bandwidth is achieved. The VSWR is less than 2 within the frequency range from 6.1 GHz to 18 GHz for the simulated result and 6.3 GHz to 18.8 GHz for the measured one. The

discrepancy may be due to the small air gap existing between the Teflon and ceramic slab in our prototype. In addition, fabrication and assembling tolerances may also attribute to the difference.

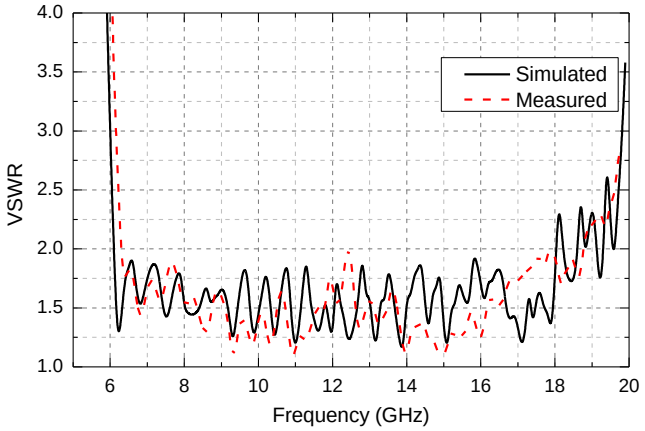

Fig. 11. Simulated and measured VSWR of the proposed surface wave antenna.

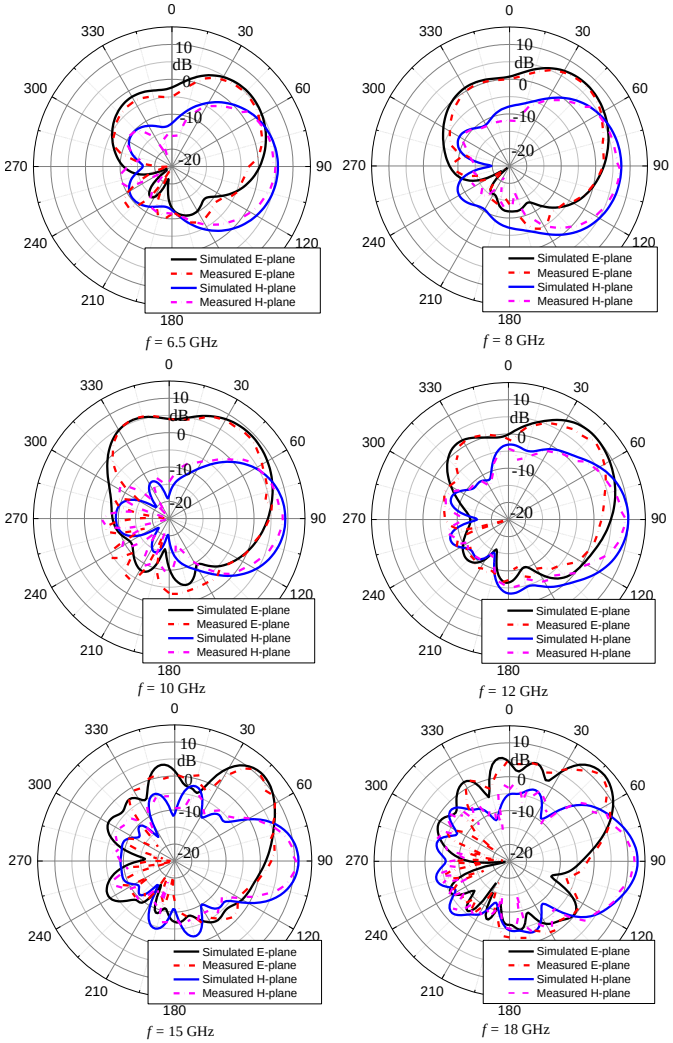

Fig. 12 Simulated and measured radiation patterns of the proposed surface wave antenna at different frequencies.

Radiation patterns of the proposed antenna are measured in the anechoic chamber, as depicted in Fig. 12. The results show that the simulated and measured patterns of both E- and H-plane are in good agreement. The radiation beam angle in the E-plane is about 45°away from the end-fire direction over the frequency range due to the existence of the finite ground. As discussed in Section III, the finite ground has significant influence on the radiation beam angle. The ratio of the ground length *Lg* that starts from the resonant point where the radiation occurs till the end of the slab to the free-space wavelength is almost identical at different frequencies. Therefore, the beam angles are almost stable since the ground effect is almost the same over the entire band.

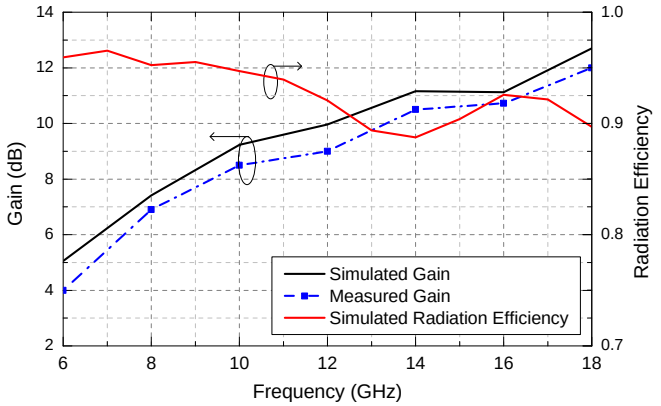

Fig. 13 Simulated and measured gain values and simulated radiation efficiency of the proposed surface wave antenna.

Fig. 13 shows the gain values and simulated radiation efficiency over the operation bandwidth. The simulated gain is 5.1 dB at 6 GHz, and increases to 12.8 dB at 18 GHz. The measured gain values are slightly less than the simulated ones; and the gain discrepancies are within the range of 0.5 dB to 1 dB over the entire frequency band. It is expected that the insertion loss of the SMA connector is around 0.2 dB. The actual loss tangent of the commercial ceramic material is slightly larger than the one used in simulations, which also results in around 0.2 dB gain degradation. The other unpredictably slight discrepancy may be due to the fabrication and assembling tolerances, and the alignment error of our measurement setup. The radiation efficiency is calculated using G/D, where G denotes the gain and D is the directivity of the antenna. The values are obtained by the simulated results in HFSS. As shown, the radiation efficiency is above 88% over the entire operation bandwidth.

Furthermore, it is worth noting that a larger ground plane can tilt the beam angle closer to the end-fire direction. If the ground plane is infinite, an ideal end-fire radiation pattern may be obtained. In order to examine the effects of the ground size on the antenna's radiation pattern, the ground plane of the proposed antenna is extended beyond the end of the slab along the +y direction, and the effect of different ground sizes on the radiation pattern is illustrated in Fig. 14. It is seen that when the extended ground length increases from 1λ to 10λ, the beam angle of the patterns in the E-plane can be gradually tilted from around 45° to 30°away from the end-fire direction.

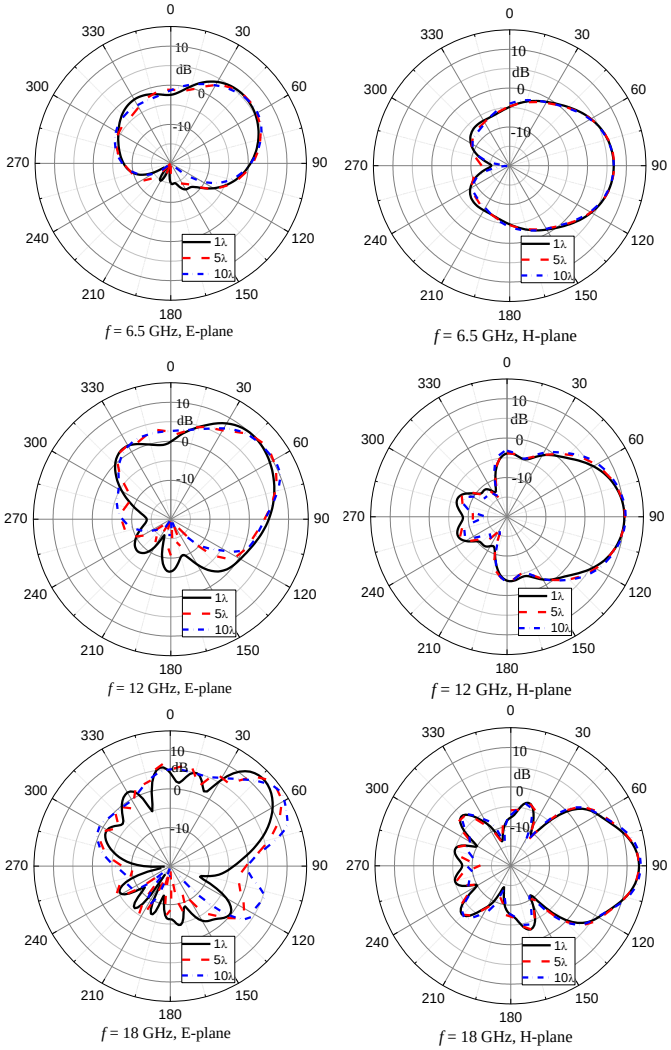

Fig. 14 Simulated radiation patterns of the proposed surface wave antenna with different lengths of an extended ground plane.

TABLE II
PERFORMANCE COMPARISON OF FLUSH-MOUNTABLE END-FIRE ANTENNAS

Reference	Bandwidth (VSWR ≤ 2)	Dimensions (λ_0) ($L\times W\times H$, λ_0 is the wavelength at the center frequency)	Volume (λ_0^3)	Gain at the center frequency (dB)
[7]	10%	6.7 ×11.5 ×0.17	13.1	-
[13]	19%	1.56 ×1.26 ×0.1	0.19	7.1
[15]	66.7%	10 ×4.8 ×0.29	13.92	10
[16]	120%	9 ×4.3 ×0.32	12.38	9.5
[17]	76%	6.7 ×3.8 ×0.25	6.365	7.8
Our work	100%	3.2 ×1.16 ×0.12	0.45	9

Table II summaries the performance comparison of several flush-mountable end-fire antennas. It is seen that although the antenna in [13] can maintain a slightly lower thickness and a compact size than our proposed antenna, the bandwidth is significantly narrower. Meanwhile, the design in [16] can achieve a wider bandwidth, but the size is big and the thickness is much larger. Therefore, our proposed antenna has the advantages of wide bandwidth, low profile as well as compact size over other flush-mountable end-fire antennas.

V. CONCLUSION

In this paper, a wideband, low-profile, and compact surface wave antenna has been presented. The surface wave is radiated at the position of the tapered grounded slab where the slab thickness is equal to $\lambda/4\sqrt{\varepsilon_r}$. A unidirectional surface wave launcher with a broad bandwidth and quasi-plane waves at the aperture of the launcher has been realized by utilizing a probe-fed parallel-plate waveguide with a modified parabolic reflecting wall and a metallic post. The procedures of designing the tapered slab and surface wave launcher have been also provided. Besides the advantages of wideband, low-profile and compact size, the antenna can obtain stable radiation patterns, moderate gain, and high radiation efficiency over the entire frequency range. It is worth mentioning that the proposed antenna is suitable to be mounted on the surfaces of aircrafts and can be readily extended to conformal arrays.

REFERENCES

[1] D. E. Isbell, "Log periodic dipole array," *IRE Trans. Antennas Propog*., vol. 8, no. 3, pp. 260–267, May 1960.

[2] G. A. Thiele, "Analysis of Yagi-Uda-type antennas," *IEEE Trans. Antennas Propag*., vol. 17, no. 1, pp. 21–30, Jan. 1969.

[3] J. Ramakrishna and D. Schaubert, "Analysis of the tapered slot antenna," *IEEE Trans. Antennas Propag*., vol. 35, no. 9, pp. 1058–1065, Sep. 1987.

[4] A. Roederer, "A log-periodic cavity-backed slot array," *IEEE Trans. Antennas Propag.*, vol. 16, no. 6, pp. 756–758, Nov. 1968.

[5] K. C. Kelly and R. S. Elliott, "Serrated waveguide—Part II: Experiment," *IRE Trans. Antennas Propag*., vol. 5, no. 3, pp. 276–283, Jul. 1957.

[6] T. F. Carberry, "Beam tilt-angle compensation for a rotatable flush-mounted surface-wave antenna on an asymmetrical ground plane," *IEEE Trans. Antennas Propag*., vol. 16, no. 1, pp. 135–136, Jan. 1968.

[7] R. Yang, Z. Lei, L. Chen, Z. Wang, and Y. Hao, "Surface wave transformation lens antennas," *IEEE Trans. Antennas Propag.*, vol. 62, no. 2, pp. 973–977, Feb. 2014.

[8] J. L. Volakis, *Antenna Engineering Handbook*, 4th ed. New York: McGraw-Hill, 2007.

[9] D. Sievenpiper, L. Zhang, R. F. J. Broas, N. G. Alexopolous, and E. Yablonovitch, "High-impedance electromagnetic surfaces with a forbidden frequency band," *IEEE Trans. Microw. Theory Tech*., vol. 47, no. 11, pp. 2059–2074, Nov. 1999.

[10] H. F. Hammad, Y. M. M. Antar, A. P. Freundorfer, and S. F. Mahmoud, "Uni-planar CPW-fed slot launchers for efficient TM_0 surface-wave excitation," *IEEE Trans. Antennas Propag.*, vol. 51, no. 4, pp. 1234–1240, Apr. 2003.

[11] S. K. Podilchak, A. P. Freundorfer, and Y. M. M. Antar, "Surface-wave launchers for beam steering and application to planar leaky-wave antennas," *IEEE Trans. Antennas Propag.*, vol. 57, no. 2, pp. 355–363, Feb. 2009.

[12] R. E. Collin, *Field Theory of Guided Waves*, New York: McGraw Hill, 1960.

[13] M. E. Morote, B. Fuchs, J. F. Zurcher, and J. R. Mosig, "Novel thin and compact H-plane SIW horn antenna," *IEEE Trans. Antennas Propag*., vol. 61, no. 6, pp. 2911-2920, Jun. 2013.

[14] Y. Zhao, Z. Shen, and W. Wu, "Wideband and low-profile H-plane ridged SIW horn antenna mounted on a large conducting plane," *IEEE Trans. Antennas Propag.*, vol. 62, no. 11, Nov. 2014.

[15] B. T. Stephenson and C. H. Walter, "Endfire slot antennas," *IRE Trans. Antennas Propag*., vol. 3, no. 2, pp. 81-86, Apr. 1955.

[16] J. W. Eberle, C. A. Levis, and D. McCoy, "The flared slot: A moderately directive flush-mounted broad-band antenna," *IRE Trans. Antennas Propag*., vol. 8, no. 5, pp. 461-468, Sep. 1960.

[17] A. R. Mallahzadeh and S. Esfandiarpour, "Wideband H–plane horn antenna based on ridge substrated integrated waveguide (RSIW)," *IEEE Antenna Wireless Propag. Lett*., vol. 11, pp. 85-88, 2012.

[18] D. M. Pozar, *Microwave Engineering*, 3rd ed. New York: Wiley, 2005.

[19] S. S. Attwood, "Surface-wave propagation over a coated plane conductor," *J. Appl. Phys*., vol. 22, no. 4, pp. 504-509, Apr. 1951.

[20] F. E. Butterfield, "Dielectric sheet radiators," *IRE Trans. Antennas Propag*., vol. 2, no. 4, pp. 152–158, Oct. 1954.
[21] C. A. Balanis, *Antenna Theory Analysis and Design*, 3rd ed. New York: Wiley, 2005.
[22] L. B. Felsen, "Radiation from a tapered surface wave antenna," *IRE Trans. Antennas Propag*., vol. 8, no. 6, pp. 577–586, Nov. 1960.
[23] Z. Hu and Z. Shen, "Reconfigurable leaky-wave antenna based on periodic water grating," *IEEE Antennas Wireless Propag. Lett.*, vol. 13, pp. 134–137, 2014.
[24] M. Sato, Y. Konishi, and S. Urasaki, "A traveling-wave fed parallel plate slot array antenna with inclined linear polarization at 60 GHz," *10th Int. Conf. Antennas Propagat. (ICAP)*, 1997, pp. 14-17.
[25] Y. J. Cheng, W. Hong, and K. Wu, "Millimeter-wave substrate integrated waveguide multibeam antenna based on the parabolic reflector principle," *IEEE Trans. Antennas Propag*., vol. 56, no. 9, pp. 3055-3058, Sep. 2008.
[26] E. Alfonso and P. S. Kildal, "Parabolic cylindrical reflector antenna at 60 GHz with line feed in gap waveguide technology," *7th Eur. Conf. Antennas Propagat. (EuCAP)*, 2013, pp. 319–323.
[27] H. F. Hammad, Y. M. M. Antar, A. P. Freundorfer, and M. Sayer, "A new dielectric grating antenna at millimeter wave frequency," *IEEE Trans. Antennas Propag.*, vol. 52, no. 1, pp. 36–44, Jan. 2004.
[28] T. Tamir and S. T. Peng, "Analysis and design of grating couplers," *Appl. Phys*., vol. 14, no. 3, pp. 235–254, Feb. 1977.
[29] R. E. Collin, *Foundations for Microwave Engineering*, New York: McGraw-Hill, 1966.

Zhuozhu Chen (S'13) was born in Hunan province, China. He received the B.Eng. degree and the M.S. degree in electronic engineering from Beijing Institute of Technology, China, in 2010 and 2013, respectively. He is currently working toward the Ph.D. degree in electrical and electronic engineering at Nanyang Technological University, Singapore.

His research interests include design of RF/microwave antennas and circuit.

Zhongxiang Shen (M'98-SM'04) received the B. Eng. degree from the University of Electronic Science and Technology of China, Chengdu, China, in 1987, the M. S. degree from Southeast University, Nanjing, China, in 1990, and the PhD degree from the University of Waterloo, Waterloo, Ontario, Canada, in 1997, all in electrical engineering.

From 1990 to 1994, he was with Nanjing University of Aeronautics and Astronautics, China. He was with Com Dev Ltd., Cambridge, Canada, as an Advanced Member of Technical Staff in 1997. He spent six months each in 1998, first with the Gordon McKay Laboratory, Harvard University, Cambridge, MA, and then with the Radiation Laboratory, the University of Michigan, Ann Arbor, MI, as a Postdoctoral Fellow. In 1999, he joined Nanyang Technological University (NTU), Singapore, as an assistant professor. He has been an associate professor in the School of Electrical and Electronic Engineering, NTU, since Jan. 2004.

Dr. Shen is a member of the Antennas and Propagation and Microwave Theory and Techniques Societies of the IEEE. He served as Chair of the IEEE MTT/AP Singapore Chapter. He was as the Chair of AP-S Chapter Activities Committee from Jan. 2010 to Aug. 2014. He is currently serving as the Secretary of IEEE AP-S.

His research interests include design of small and planar antennas for various wireless communication systems, analysis and design of frequency-selective structures and absorbers, hybrid numerical techniques for modeling RF/microwave components and antennas. He has authored or co-authored more than 130 journal papers and presented another 120 conference papers.